Oral presentation | Incompressible/compressible/hypersonic flow

Incompressible/compressible/hypersonic flow-II

Wed. Jul 17, 2024 4:30 PM - 6:30 PM Room D

[9-D-04] Influence of Ablation on Laminar-Turbulent Transition over Compression Ramp at Mach 8

*Ata Onur Baskaya[1], Stefan Hickel[1] （1. Faculty of Aerospace Engineering, Delft University of Technology, Delft, The Netherlands）

Keywords: Hypersonic flow, Laminar-turbulent transition, Ablation

Twelfth International Conference on Computational Fluid Dynamics (ICCFD12), Kobe, Japan, July 14-19, 2024

Baroclinic Shift of Hypersonic Heating Streaks over an Ablating Compression Ramp

A. O. Başkaya* and S. Hickel*
Corresponding author: a.o.baskaya@tudelft.nl
* Delft University of Technology, 2629HT Delft, The Netherlands.

Abstract: We present novel observations from Direct Numerical Simulations (DNS) of transitional Mach 8 flow over a 15° compression ramp ablator. Heating streaks over the ramp are seen to undergo a phase shift of 180° near the location of transition from laminar to turbulent boundary layer flow. This phenomena leads to a drastic change of the surface ablation pattern. Our analysis shows that the underlying mechanism behind this phenomenon is the baroclinic torque in the strongly stratified near-wall region. We discuss the impact of this *baroclinic shift* for a surface undergoing ablative recession.

Keywords: Hypersonic Flows, Baroclinic Torque, Ablation, Gas-Surface Interactions, Computational Fluid Dynamics.

1 Introduction

Streamwise vortices emerging from flow instabilities driven by streamline curvature and shock-wave boundary layer interactions are ubiquitous in high-speed flows. From control surfaces to engine intakes, many configurations exhibit these vortical structures [1]. Through the lift-up mechanism, these vortices induce spanwise variations in the flow field and especially in the surface quantities. They influence the species concentrations in a reacting boundary layer by carrying mass, the flow dynamics by transporting momentum, and the surface heat load by advecting energy. Peak heating rates and locations can be substantially altered by the formation and evolution of the streamwise streaks [2]. Developing a detailed understanding of these interactions is crucial to predict their occurrence during the flight of high-speed aircraft and spacecraft. The generation of these streamwise vortices has been attributed to several different mechanisms including convective and intrinsic instabilities [3], which can destabilize the laminar flow and eventually trigger transition to turbulence. Of particular interest to the current work, one such mechanism studied recently by Zapryagaev *et al.* [4] and Dwivedi *et al.* [5] is governed by baroclinic effects due to the interaction of strong wall-normal density gradients with transversal pressure gradients.

Counting the aforementioned works, influential studies concerned with the formation of streamwise vortices proceeding reattachment [6] and within the recirculation bubble [7] are not scarce. However, often due to limitations imposed by ground-testing facilities [8, 9], previous studies considered almost exclusively (see work of Egorov *et al.* [10]) short ramp lengths of only one L, where L is the distance from the leading edge to the ramp corner [3, 6, 7, 11, 12]. Owing to this compact setup becoming canonical for fundamental research on such interactions, the downstream development of the transitional streaks have been frequently overlooked.

The specific aim of this present study is the influence of persistent vortex structures, their evolution, and the effect of the resulting streak pattern in the context of thermal protection systems and space debris, where the surface of the object is eroding away due to gas-surface interactions (GSI) such as ablation. To this end, we consider a 15° compression ramp configuration exposed to Mach 8 flow and a ramp length of approximately $3L$. Different pattern of ablation, such as cross-hatching, have been observed in wind-tunnel experiments as well as on recovered objects that have survived atmospheric entry [13]. The effect of these pattern on the heat load and the boundary-layer stability is a complex multi-physics problem with many unknowns and is not yet well understood.

This paper presents our observations of a novel phenomena and a proposed physical interpretation. We report the emergence of a streamwise vortex structure that causes a drastic shift in the heating streaks over the compression ramp in Section 3.2. We discuss the sensitivity of this interaction to inflow perturbation amplitudes in Section 3.3 and its impact on surface ablation in Section 3.4. Concluding remarks are given in Section 4.

2 Governing Equations and Numerical Methods

We solve the compressible Navier-Stokes equations for a multispecies chemically-inert fluid

$$\frac{\partial \vec{U}}{\partial t} + \vec{\nabla} \cdot \vec{F}(\vec{U}) = \vec{S}\,, \tag{1}$$

where $\vec{U} = [\rho_i, \rho u, \rho v, \rho w, \rho E]^{\mathrm{T}}$ is the vector of conserved variables, $\vec{F} = \vec{F}_{inv} + \vec{F}_{vis}$ is the sum of inviscid and viscous fluxes, and $\mathbf{S}$ is the vector of source terms. Along the x axis, they are:

$$\vec{F}_{inv} = \begin{bmatrix} \rho_i u \\ \rho u^2 + p \\ \rho u v \\ \rho u w \\ u(\rho E + p) \end{bmatrix}, \quad \vec{F}_{vis} = \begin{bmatrix} J_{\mathrm{x},i} \\ -\tau_{\mathrm{xx}} \\ -\tau_{\mathrm{xy}} \\ -\tau_{\mathrm{xz}} \\ -(\tau_{\mathrm{xx}} u + \tau_{\mathrm{xy}} v + \tau_{\mathrm{xz}} w) + q_{\mathrm{x}} \end{bmatrix}, \tag{2}$$

where ρ_i is the species partial density for the i^{th} species, $\vec{u}$ is the mixture average velocity, ρ is the mixture density, p is the mixture pressure, and $E = e + u^2/2$ is the specific total energy, which is the sum of the thermodynamic internal energy e and the kinetic energy. Note that the species source terms in $\vec{S}$ are taken as zero as no homogeneous gas-phase reactions are occurring at the conditions studied in this work. Modeling approaches for the species diffusion flux $\vec{J}_i$, the viscous stress tensor $\vec{\tau}$, and the total heat flux $\vec{q}$ are detailed in Başkaya *et al.* [14].

Single species air is used for the simulations with an inert wall. Gas viscosity is modeled by Sutherlands's law, specific heats are taken to be constant, and thermal conductivity is obtained from a Prandtl number of 0.72. When camphor is introduced due to the ablative boundary condition, cubic polynomials for viscosity and thermal conductivity presented by Zibitsker *et al.* [15] are employed with a unit Prandtl number. Lewis number is taken as unity for camphor diffusion.

The governing equations are solved with our in-house solver, INCA, which is a high-fidelity finite-volume solver for Direct Numerical Simulations (DNS) and Large Eddy Simulations (LES) of the compressible chemically reacting Navier-Stokes equations and provides a large number of different discretization schemes on three-dimensional block-Cartesian AMR grids [16, 17, 18]. For the purposes of this study, a third-order weighted essentially non-oscillatory (WENO) scheme [19] with HLLC flux function [20] is selected for the hyperbolic flux. Second-order centered differences are used for the viscous terms and the explicit third-order Runge-Kutta scheme of Gottlieb and Shu [21] is selected for time integration. The ramp wall is represented by a cut-element immersed boundary (IB) method [22], which is a consistent and conservative extension of the finite-volume flux balance. This approach accurately accounts for mesh cells being split by flow boundaries. Boundary conditions are imposed on the cut-elements that result from the intersection of the Cartesian fluid grid and the surface triangulation of the solid. Details of this method and its extension to reacting immersed boundaries have been presented by Başkaya *et al.* [23, 24].

The GSI boundary condition makes use of the open-source Mutation^{++} library [25]. We solve for the mass blowing rate $\dot{m} = \sum_i \dot{\omega}_{i,wall}$, calculated as the sum of the species source term $\dot{\omega}_{i,wall}$. The speed at which ablation products blow out of the surface is $v_{blow} = \dot{m}/\sum_i \rho_i$. Values obtained for species densities and mass blowing speeds are imposed as boundary conditions for the Navier-Stokes equations. Similarly, the speed at which the surface recesses is $v_{wall} = \dot{m}/\rho_s$, where ρ_s is the solid density.

With an inert wall, the source term $\vec{S}$ in Eq. 1 is only due to the forcing applied to perturb the laminar base flow. The GSI boundary condition additionally introduces $\dot{\omega}_{i,wall}$ for the mass conservation, $\dot{m}\,(\mathbf{v}_{blow} \cdot \mathbf{n})$ with the surface normal vector $\vec{n}$ for the momentum conservation, and $\dot{m}\left(h + \frac{1}{2}\|\,\vec{v}_{blow}\,\|^2\right)$ with mixture enthalpy h for the energy conservation source terms.

The surface recession is orders of magnitude slower than characteristic time scales of the fluid flow. To achieve a sufficient amount of shape change within a reasonable wall-clock time, it is common practice in simulations with ablative recession to accelerate the recession speed. We have found that accurate representation of physicochemistry and fluid dynamics is ensured with an acceleration factor of 10^5 [14].

Table 1: Freestream conditions for the considered compression ramp.

M_∞	P_∞ [Pa]	T_∞ [K]	T_{wall} [K]	$Re_L(10^5)$
8	355	55	293	3.7

3 Analysis of the *Baroclinic Shift*

3.1 Numerical Setup and Observations

Our analysis begins by setting up numerical experiments inspired by the works of Chuvakhov *et al.* [26] and Dwivedi *et al.* [5]. Validation of the numerical predictions based on these results in literature has been presented by Başkaya *et al.* [14]. Unlike both of these past studies, we will consider an extended domain approximately double the length in the streamwise direction. The compression ramp geometry consists of a flat plate with a length of $L = 0.05$ m that is aligned with the Mach 8 free-stream flow, followed by a 15° wedge until 0.195 m in the streamwise direction. The spanwise width of the domain is 0.003 m to capture one wavelength of the most unstable mode found by Dwivedi *et al.* [5]. Volume forcing is applied between 0.02 m and 0.023 m to perturb the flow, following Başkaya *et al.* [14]. Inflow conditions, see Table 1, are supplied at the sharp leading edge of the flat plate. Top and right-most boundaries are set as non-reflecting zero-gradient outflow and periodic boundary conditions are applied in the spanwise direction. An inert isothermal wall boundary condition with a temperature of 293 K is assigned to the ramp surface.

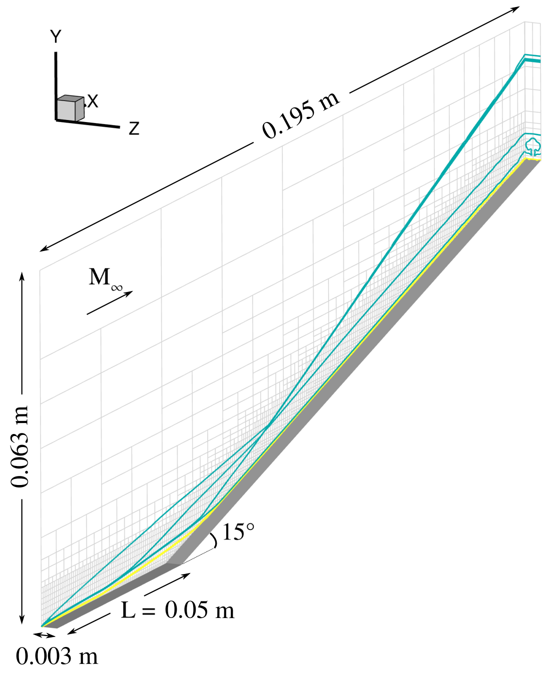

Figure 1: Sketch of the compression ramp geometry with the AMR block structure of the Cartesian grid. Mach number contours are plotted with blue lines and the sonic line is highlighted in yellow.

Initial perturbations grow to develop into steady streamwise vortex-streak system. The vortex formation is visualized in Fig. 2. It can be observed from the figure, counter-rotating vortices grow to a significant amplitude as the flow reattaches on the ramp and evolve as they travel downstream. Formation of secondary vortices surrounding the streaks signal the onset of transition and the eventual turbulent breakdown. These stages are highlighted in Fig. 2.

The lift-up effect results in alternating hotter and colder streaks along the ramp's surface, as shown in Fig. 3. These thermal streaks are most discernible downstream of the reattachment point. An intriguing observation can be made from the near-wall streak patterns in Fig. 3. Traveling downstream after reattachment, the streak pattern undergoes an abrupt variation: the regions of heating and cooling

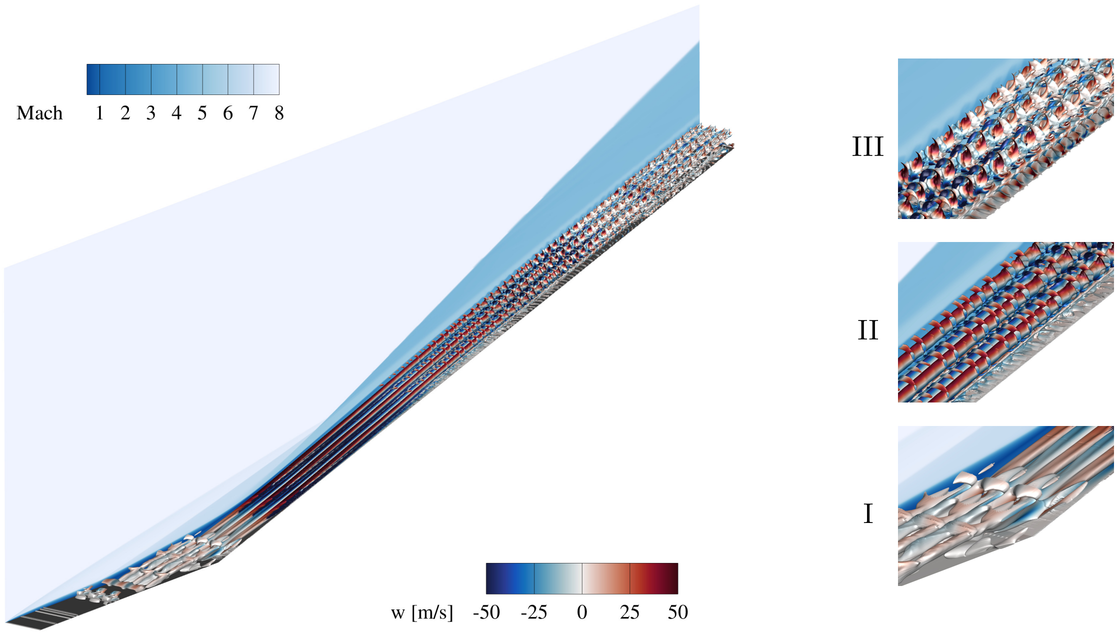

Figure 2: Isometric view of the domain with a Q-criterion iso-surface contoured with the spanwise velocity. Background slice in the spanwise direction shows Mach number contours. Three close-up views on the right hand side focus on (I) the steady streaks reattaching on the ramp surface, (II) onset of transition, and (III) the turbulent breakdown.

interchange near $x = 0.13$ m. This shift is more clearly noticeable from the contours of streamwise velocity plotted at a wall distance of 10 µm, as shown in the same figure. Beyond the shift, momentum deficit streaks become momentum excess streaks. This suggests the existence of a vortex pair close to the wall that is phase shift by 180° compared to the vortex orientations near reattachment. We will refer to this point where the vortices seemingly "reverse" as the location of *baroclinic shift*, since we believe, as the rest of this discussion will attempt to elucidate, this shift is caused by baroclinic effects.

To aid the investigation, we present spanwise velocity, temperature, and density distributions on streamwise slices at $x = [0.06474, 0.08684, 0.1089, 0.1311]$ m in Fig. 4. These 4 slices are located between reattachment and the baroclinic shift. We can immediately distinguish a vortex structure in the first (leftmost) slice for spanwise velocity contours. The colormap is selected as such to discern the smallest occurrences. In the next slice we can already see the emergence of a secondary vortex near the surface. In subsequent slices this secondary vortex grows and evolves near the surface. What we observe in these slices directly reflects the shift in the patterns in Fig. 2. Comparing the first and the last slices, we observe the formation of a secondary vortex pair close to the wall with an opposite orientation to the primary vortices.

3.2 Physical Interpretation

To understand this phenomenon, let us examine the other quantities in Fig. 4. In the temperature slices we can clearly see the "mushroom" structure generated by the lift-up effect. The high temperature flow past the shock is entrained into the near-wall region by these vortices. Following the slices downstream, we see that the flow gradually cools down. This happens rapidly for the vortices away from the wall as the lift-up effect promotes mixing with the cold freestream. The cold isothermal wall near the surface influences the flow in a similar manner. As a result, at a certain instance the only region left with higher temperatures between two colder layers is a thin region trapped between the surface and the outer flow. This leads to lower densities in this region as can be seen from the slices of density variations in Fig. 4. This is a critical observation as this variation in the wall normal direction reverses the direction of the density gradient through this layer.

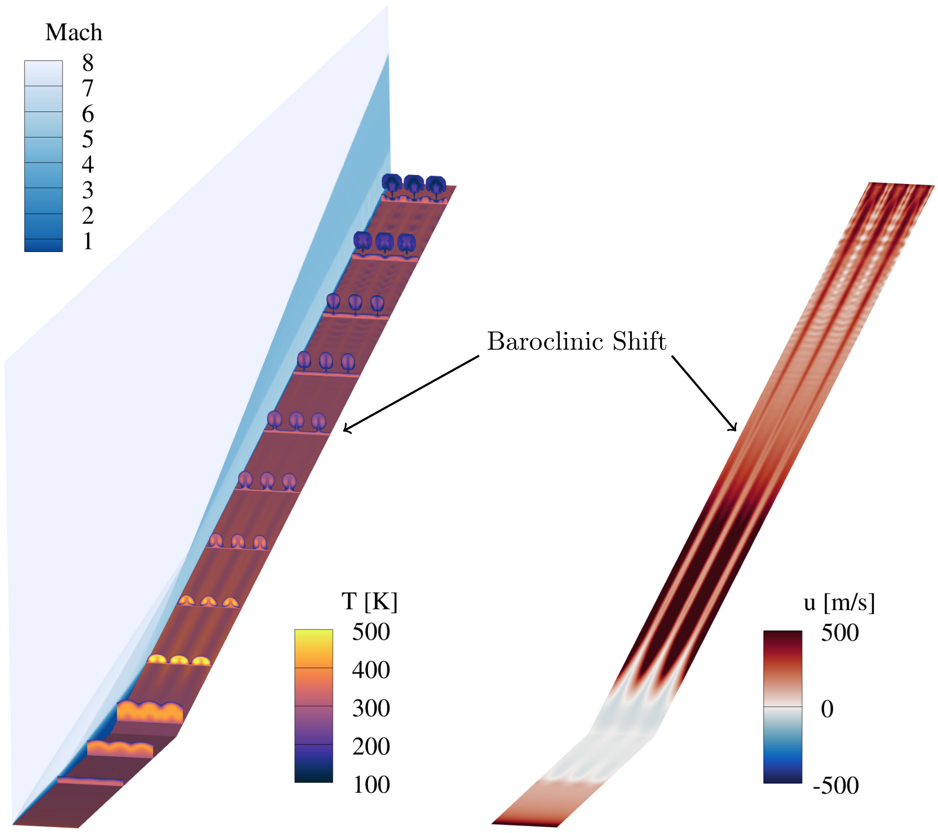

Figure 3: Isometric view of streamwise slices showing the spatial evolution of temperature contours. The spanwise background slice shows Mach number contours. The ramp surface is also contoured by temperature (on the left) and streamwise velocity (on the right).

Figure 5 focuses on the region near the surface and shows the density variations for the slice at $x = 0.1311$ m. The slice domain is extended in the spanwise direction to include one more streak for visualization purposes. In the topmost slice, pressure contour lines (white) are overlaid on density contour fields. In the subsequent slices, black lines represent density contour lines. We can observe from the first two slices the variations in density and pressure. It is clear that the changes in these quantities leads to a density gradient $\nabla\rho$ in the wall normal direction and a pressure gradient ∇p in the spanwise direction. The misalignment of these two gradients leads to a baroclinic torque $\nabla\rho \times \nabla p$. This term is plotted as $\mathrm{T}_b = (\nabla\rho \times \nabla p)/\rho^2$ in the same figure. Streamwise vorticity is also included to show that this component is in the same direction as the baroclinic term. Observe that the thin region of lower density (the "trapped" flow) that we have identified earlier leads to a density gradient in the direction pointing away from the surface above a certain height and a density gradient in the opposite direction near the wall. With the pressure gradient direction remaining the same above and below the thin region, the baroclinic torque has the opposite direction above and below the region of the trapped flow. The effect of this can also be seen when we look at the evolution of baroclinic torque and streamwise vorticity in Fig. 6 at the same locations shown in Fig. 4. In the first slice, the reattachment streaks are promoted by the baroclinic torque. In the following slices, the baroclinic term near the wall favors the emerging vortices in the opposite orientation. This can also be examined from a spanwise slice at $z = 1.4$ mm in Fig. 7. The baroclinic torque opposes the vorticity of the preexisting streamwise vortices and produces streamwise vorticity with opposite sign around $n_x = 0.115$ m in the wall tangent coordinate system prior to the onset of transition. This confirms that baroclinic torque is the mechanism that generates the alternating streak patterns shown in Fig. 3.

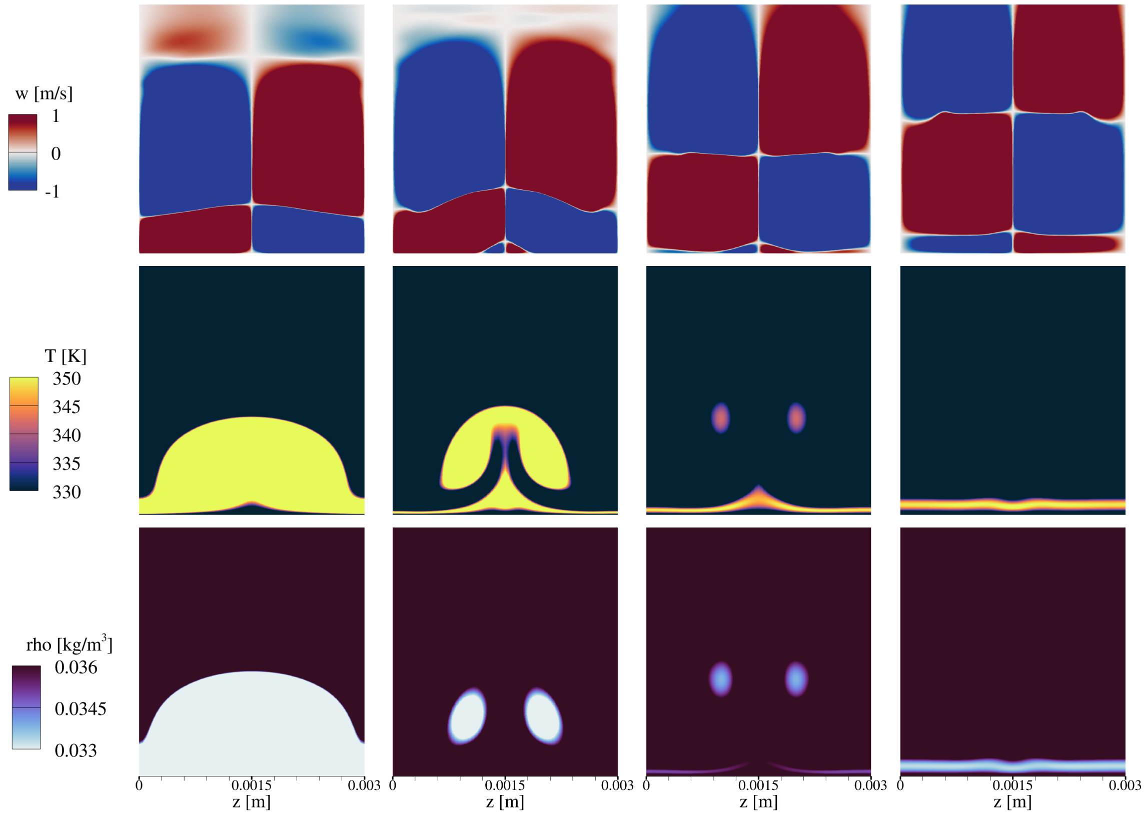

Figure 4: Streamwise slices along the ramp at $x = [0.06474, 0.08684, 0.1089, 0.1311]$ plotting spanwise velocity, temperature, and density variations. Horizontal axis is the spanwise direction. Flow direction is pointing inwards.

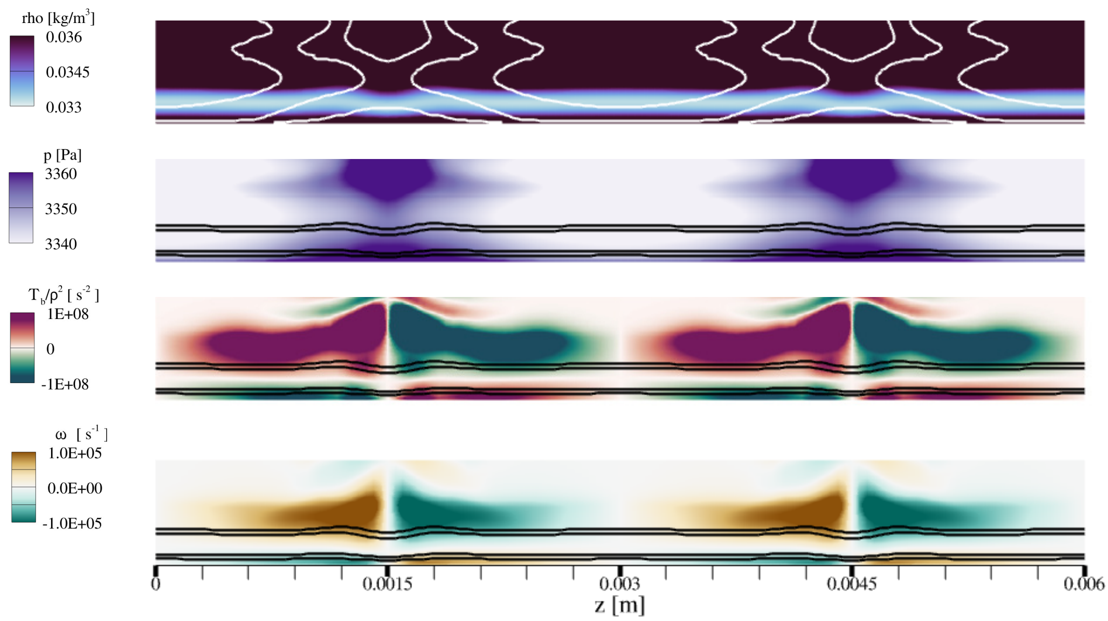

Figure 5: Streamwise slice at $x = 0.1311$ showing density, pressure, baroclinic torque, and vorticity distributions. Pressure contour lines are plotted in white and density contour lines are plotted in black. Horizontal axis is the spanwise direction. Flow direction is pointing inwards.

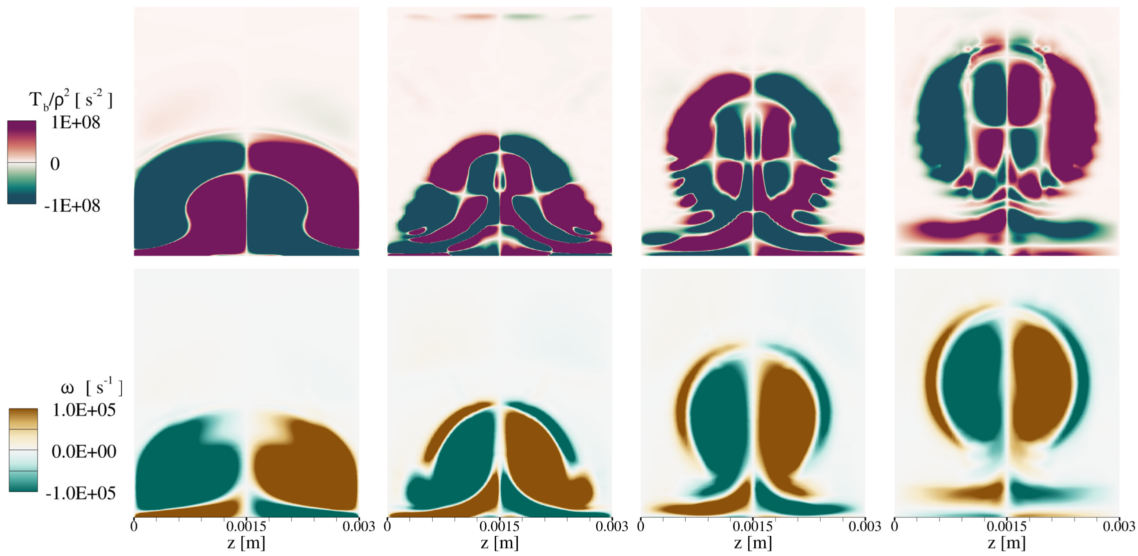

Figure 6: Streamwise slices along the ramp at $x = [0.06474, 0.08684, 0.1089, 0.1311]$ plotting spanwise velocity, temperature, density, and pressure variations. Horizontal axis is the spanwise direction. Flow direction is pointing inwards.

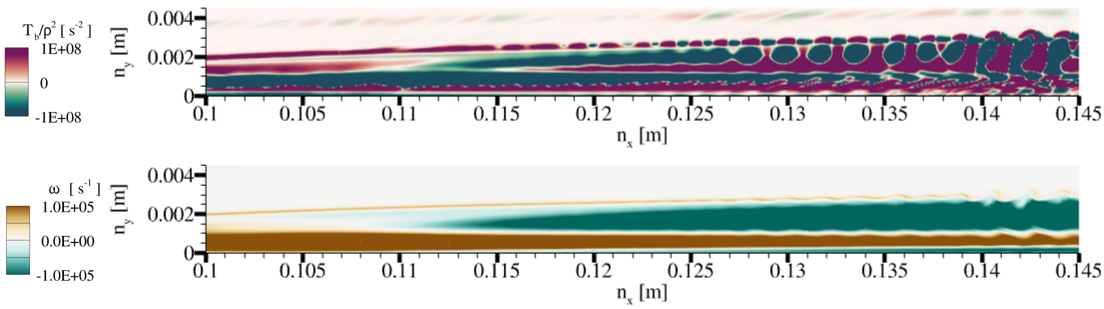

Figure 7: Spanwise slices along the ramp at $z = 1.4$ mm plotting streamwise baroclinic torque and streamwise vorticity in the wall coordinates.

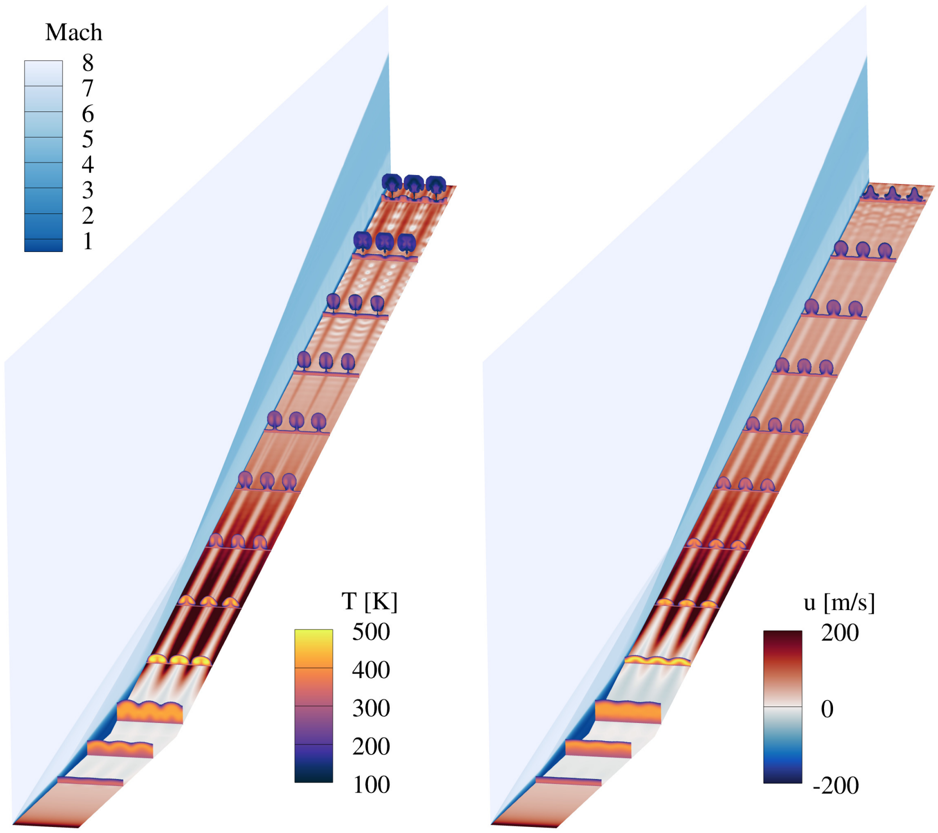

Figure 8: Isometric view of streamwise slices showing the spatial evolution of temperature contours for the high (left) and low (right) amplitude perturbations. The spanwise background slice shows Mach number contours. The ramp surface is contoured streamwise velocity.

3.3 Sensitivity to Perturbation Amplitude

To assess the sensitivity of the results to the perturbation amplitudes, we have performed the same simulations with 30% of the forcing amplitude used in the preceding simulations. The resulting flow fields for the high and low amplitude perturbations are presented in Fig. 8. The low amplitude case does not show the reversal of the near wall streaks. With a lower initial perturbation, reattachment, and the resulting streaks, occur farther downstream as can be seen from the expanded recirculation region. The lift-up effect and therefore the density gradient across the trapped flow in the boundary layer is weaker compared to the high amplitude case. The production of the opposing baroclinic torque is not sufficiently strong to emerge beneath the initial streaks before the flow begins breaking down to turbulence.

Figure 9 shows the streamwise distribution of Stanton numbers

$$St = \frac{q_{wall}}{\rho_\infty U_\infty c_p (T_r - T_{wall})} \tag{3}$$

calculated along the surface of the ramp at $z = 1.5$ mm and $z = 0.0$ mm for high and low amplitude cases. A recovery factor of 0.846 was used in the calculation of the recovery temperature T_r. The specific heat at constant pressure is taken as $c_p = 1005$ J/(kg·K). Note that $z = 1.5$ mm corresponds to the center of the lift-up. At reattachment, a higher peak heat flux is observed along $z = 0.0$ mm compared to $z = 1.5$ mm and downstream the heat flux gradually decreases, as can be tracked from Fig. 3. Along the lift-up for the high amplitude case, however, an initial peak is followed by a stronger secondary peak downstream of the baroclinic shift location. This secondary peak does not exist in the low amplitude case.

3.4 Impact on an Ablating Surface

The shift in intense surface heating locations could have severe consequences for an ablative surface. To assess this, we numerically replace the rigid inert wall with a camphor wedge that can undergo

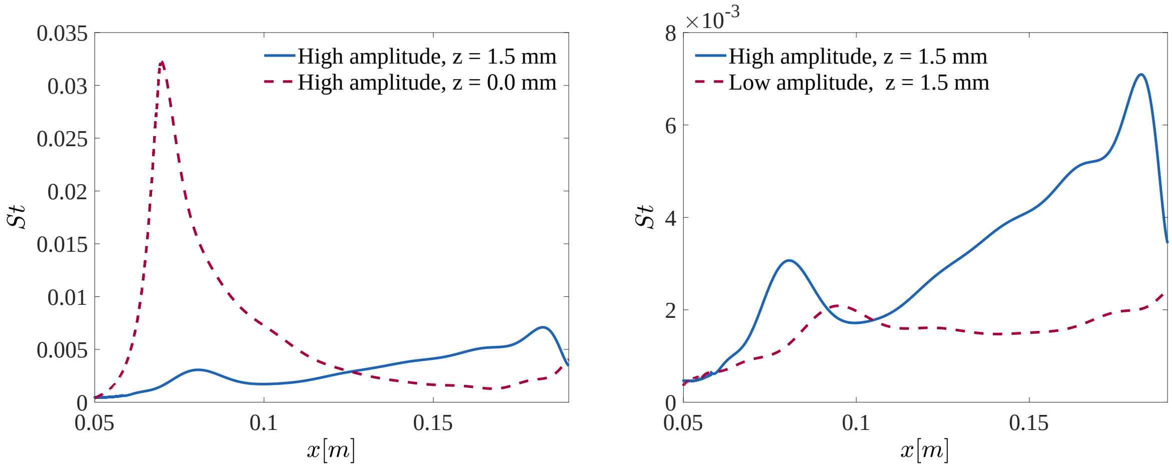

Figure 9: Streamwise distributions of Stanton number along the surface of the ramp at $z = 1.5$ mm and $z = 0.0$ mm for high and low amplitude cases.

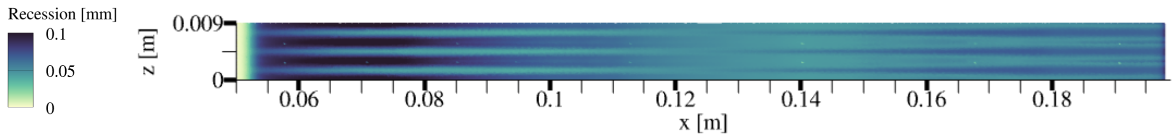

Figure 10: Recession pattern of the surface. Darker regions signify deeper grooves formed by the eroding surface material.

ablative recession. This low-temperature ablator naturally undergoes sublimation, $C_{10}H_{16}O_{(solid)} \rightarrow C_{10}H_{16}O_{(gas)}$, at these conditions. Vapor pressure and material properties for the air-camphor mixture is taken from the work of Rotondi *et al.* [27]. Details of the numerical approach employed to handle ablative recession can be found in the work of Başkaya *et al.* [14].

Employing this ablative boundary condition, we have performed simulations incorporating camphor species blowing out of the ramp and the ramp surface eroding away. Figure 10 shows a top-down view of the ramp when approximately a maximum of 0.1 mm of recession is observed. Note that ablation is smoothly ramped up from the corner of the ramp by a hyperbolic tangent function to maintain the mean ramp angle. Immediately downstream of reattachment, we can clearly distinguish how different rates of sublimation have created spanwise variations in recession. Farther downstream, beyond the baroclinic shift, the recession patterns are reversed as the secondary vortices emerge from the wall. The resulting recession pattern reflects the trend we have observed in Fig. 3.

4 Conclusions and Remarks

We have presented novel observations which include a drastically altered spanwise distribution of heating streaks formed by streamwise vortices over a compression ramp at Mach 8. We found that the dominant physical mechanism behind this phenomenon is an inversion of baroclinic production near the surface. This inversion is due to a layer of low density fluid being trapped in the boundary layer between denser fluid layers, and is produced by the lift-up effect of streamwise-vortex perturbations with sufficiently high amplitude. Downstream of the location at which the secondary vortex emerges near the wall, the surface pattern shifts due to an opposing baroclinic torque. This *baroclinic shift* has severe implications on gas-surface interactions as it changes the distribution of species concentrations and heat fluxes. The evolution of these new vortical structures promotes the inversion of the recession pattern compared to the ablation pattern generated by the heating streaks near reattachment.

References

[1] Datta V Gaitonde. Progress in shock wave/boundary layer interactions. *Progress in Aerospace Sciences*, 72:80–99, 2015.

[2] David S Dolling. Fifty years of shock-wave/boundary-layer interaction research: what next? *AIAA journal*, 39(8):1517–1531, 2001.

[3] Shibin Cao, Jiaao Hao, Igor Klioutchnikov, Chih-Yung Wen, Herbert Olivier, and Karl Alexander Heufer. Transition to turbulence in hypersonic flow over a compression ramp due to intrinsic instability. *Journal of Fluid Mechanics*, 941:A8, 2022.

[4] VI Zapryagaev, IN Kavun, and II Lipatov. Supersonic laminar separated flow structure at a ramp for a free-stream Mach number of 6. *Progress in Flight Physics*, 5:349–362, 2013.

[5] Anubhav Dwivedi, G. S. Sidharth, Joseph W. Nichols, Graham V. Candler, and Mihailo R. Jovanović. Reattachment streaks in hypersonic compression ramp flow: An input-output analysis. *Journal of Fluid Mechanics*, pages 113–135, 2019.

[6] S Navarro-Martinez and OR Tutty. Numerical simulation of Görtler vortices in hypersonic compression ramps. *Computers & fluids*, 34(2):225–247, 2005.

[7] Yi Zhuang, Hui-jun Tan, Ya-zhou Liu, Yu-chao Zhang, and Yu Ling. High resolution visualization of görtler-like vortices in supersonic compression ramp flow. *Journal of Visualization*, 20:505–508, 2017.

[8] Amit Roghelia, Herbert Olivier, Ivan Egorov, and Pavel Chuvakhov. Experimental investigation of Görtler vortices in hypersonic ramp flows. *Experiments in Fluids*, 58:1–15, 2017.

[9] G Simeonides and W Haase. Experimental and computational investigations of hypersonic flow about compression ramps. *Journal of Fluid Mechanics*, 283:17–42, 1995.

[10] Ivan Egorov, Vladimir Neiland, and Vladimir Shredchenko. Three-dimensional flow structures at supersonic flow over the compression ramp. In *49th AIAA Aerospace Sciences Meeting including the New Horizons Forum and Aerospace Exposition*, page 730, 2011.

[11] Mathieu Lugrin, Samir Beneddine, Colin Leclercq, Eric Garnier, and Reynald Bur. Transition scenario in hypersonic axisymmetrical compression ramp flow. *Journal of Fluid Mechanics*, 907:A6, 2021.

[12] Marco Marini. Analysis of hypersonic compression ramp laminar flows under sharp leading edge conditions. *Aerospace science and technology*, 5(4):257–271, 2001.

[13] S. W. Stock. Surface patterns on subliming and liquefing ablation materials. *AIAA Journal*, 13(9):1217–1223, 1975.

[14] Ata Baskaya, Sean D Dungan, Stefan Hickel, and Christoph Brehm. Fluid ablation interactions on a compression ramp at Mach 8. In *AIAA SCITECH 2024 Forum*, page 0501, 2024.

[15] Aleksander L Zibitsker, Joel A McQuaid, Christoph Brehm, and Alexandre Martin. Validation and analysis of a coupled fluid-ablation framework for modeling low-temperature ablator. *International Journal of Heat and Mass Transfer*, 218:124728, 2024.

[16] Stefan Hickel, Christian P Egerer, and Johan Larsson. Subgrid-scale modeling for implicit large eddy simulation of compressible flows and shock-turbulence interaction. *Physics of Fluids*, 26(10):106101, 2014.

[17] Vito Pasquariello, Stefan Hickel, and Nikolaus A Adams. Unsteady effects of strong shock-wave/boundary-layer interaction at high Reynolds number. *Journal of Fluid Mechanics*, 823:617–657, 2017.

[18] Muzio Grilli, Stefan Hickel, and Nikolaus A Adams. Large-eddy simulation of a supersonic turbulent boundary layer over a compression–expansion ramp. *International journal of heat and fluid flow*, 42:79–93, 2013.

[19] Guang-Shan Jiang and Chi-Wang Shu. Efficient implementation of weighted ENO schemes. *Journal of Computational Physics*, 126(1):202–228, 1996.

[20] Eleuterio F Toro. *Riemann solvers and numerical methods for fluid dynamics: a practical introduction*. Springer-Verlag, Berlin, 2013.

[21] Sigal Gottlieb and Chi-Wang Shu. Total variation diminishing Runge-Kutta schemes. *Mathematics of Computation*, 67(221):73–85, 1998.

[22] Felix Örley, Vito Pasquariello, Stefan Hickel, and Nikolaus A Adams. Cut-element based immersed boundary method for moving geometries in compressible liquid flows with cavitation. *Journal of Computational Physics*, 283:1–22, 2015.

[23] AO Baskaya and S Hickel. An accurate reconstruction and interpolation scheme for a conservative cut-cell immersed boundary method with gas-surface interactions. *14th International ERCOFTAC*

Symposium on Engineering Turbulence Modelling and Measurements (ETMM14), 2023.

[24] Ata Onur Başkaya, Michele Capriati, Alessandro Turchi, Thierry Magin, and Stefan Hickel. Assessment of immersed boundary methods for hypersonic flows with gas-surface interactions. *Computers & Fluids*, 270:106134, 2024.

[25] James B Scoggins, Vincent Leroy, Georgios Bellas-Chatzigeorgis, Bruno Dias, and Thierry E Magin. Mutation++: Multicomponent thermodynamic and transport properties for ionized gases in c++. *SoftwareX*, 12:100575, 2020.

[26] P. V. Chuvakhov, V. Ya. Borovoy, I. V. Egorov, V. N. Radchenko, H. Olivier, and A. Roghelia. Effect of small bluntness on formation of görtler vortices in a supersonic compression corner flow. *Journal of Applied Mechanics and Technical Physics*, 58:975–989, 2017.

[27] Marco Rotondi, Mario Tindaro Migliorino, Daniele Bianchi, Pietro Pagani, and Alessandro Turchi. Numerical assessment of camphor ablation flight relevance in hypersonic wind-tunnel testing. *Journal of Spacecraft and Rockets*, pages 1–18, 2022.